ACS Catalysis

pubs.acs.org/acscatalysis
Research Article

Activity and Stability of $ZnFe_2O_4$ Photoanodes under Photoelectrochemical Conditions

Ningyan Cheng,* Leonie Kanzler, Yiqun Jiang, Andrea M. Mingers, Morten Weiss, Christina Scheu, Roland Marschall,* and Siyuan Zhang*

Cite This: ACS Catal. 2024, 14, 10789−10795
Read Online

ACCESS | Metrics & More | Article Recommendations | Supporting Information

ABSTRACT: Photoelectrochemical (PEC) water splitting is a promising energy conversion and storage technology. The development requires highly active and stable photoanodes to perform the oxygen evolution reaction (OER). Here, we investigated the activity and stability of both pristine and hydrogen-treated $ZnFe_2O_4$. Using an illuminated scanning flow cell setup, we monitored the activity and dissolution rates of $ZnFe_2O_4$ under operando PEC conditions. It was found that under PEC water oxidation conditions, $ZnFe_2O_4$ does not degrade in basic pH. Moreover, thermally reduced $ZnFe_2O_4$ shows expected higher OER activity without compromising the stability compared to the pristine one. Dissolution of $ZnFe_2O_4$ was only observed once the applied potential was more cathodic than −0.1 V vs reversible hydrogen electrode as the surface Fe^{3+} is reduced regardless of illumination.

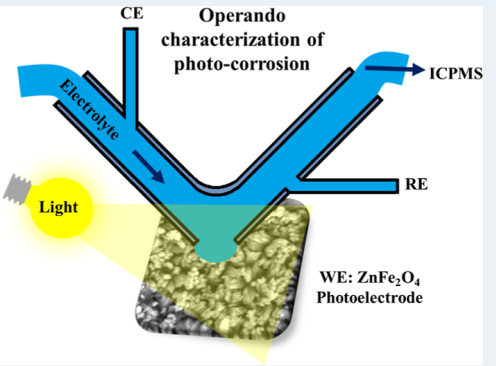

KEYWORDS: *photoelectrochemistry, water splitting, operando mass spectrometry, spinel ferrite, electrocatalyst*

INTRODUCTION

Photoelectrochemical (PEC) water splitting is one of the most attractive eco-friendly strategies for the conversion of renewable solar energy to chemical fuels.[1,2] However, despite the demonstrated impressive conversion efficiency of PEC devices, it is still challenging to develop economic, efficient, green, and robust photoelectrode materials for achieving high performance and long-term stability under harsh PEC operating conditions.[2,3] Recently, ternary materials, especially spinel ferrite with a chemical composition of MFe_2O_4 (M = Fe, Co, Zn, Mg, etc.), are drawing significant research interest, as they possess suitable band gaps for light absorption, good chemical and thermal stability, earth abundance, and low toxicity.[4−21] In particular, spinel ferrite $ZnFe_2O_4$ with a band gap of around 2 eV has been widely studied.[8,9]

Recently, it has been reported that hydrogen reduction can modify the surface ratio of Zn to Fe and generate surface oxygen vacancies, which significantly affect the charge transport and transfer properties of $ZnFe_2O_4$ and hence its PEC performance.[9,15] These studies have also demonstrated a steady photocurrent of $ZnFe_2O_4$ during PEC operation for 16 and 3 h, respectively.[9,15] Nevertheless, photocurrents are usually limited by charge carrier transport through the depth of photoelectrodes, and to ensure their long-term stability, it is indispensable to study their dissolution behavior under PEC conditions.[22] Moreover, the stable operational range for $ZnFe_2O_4$ remains to be defined, as many electrodes are prone to corrosion toward open-circuit and potential cycling conditions.[23,24] Furthermore, most literature on $ZnFe_2O_4$ photoelectrodes focuses on their stability in alkaline conditions,[9,14,15] while it is also important to examine their stability toward neutral pH. In recent years, the operando stability of many photoelectrodes has been characterized by coupling an illuminated scanning flow cell (iSFC) with an inductively coupled plasma mass spectrometer (ICPMS).[22,25−27] This technique is especially important to investigate multinary electrodes as it can separate the dissolution from different elements. For instance, it was found that Bi and V of $BiVO_4$ were dissolved at different rates when it was used as a photoanode.[22] The operando measurement is also an efficient way to screen for the stability range of photoelectrodes in different operation conditions or electrolytes.[22]

Herein, we studied the activity and dissolution behavior of pristine and hydrogen-reduced $ZnFe_2O_4$ under different operando PEC conditions by iSFC−ICPMS for the first time. It was confirmed that hydrogen reduction can improve the PEC activity of the $ZnFe_2O_4$ photoanode, resulting from the oxygen defects induced during the hydrogen treatment at

Received: April 15, 2024
Revised: June 14, 2024
Accepted: June 21, 2024
Published: July 3, 2024

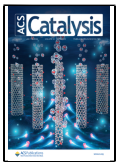

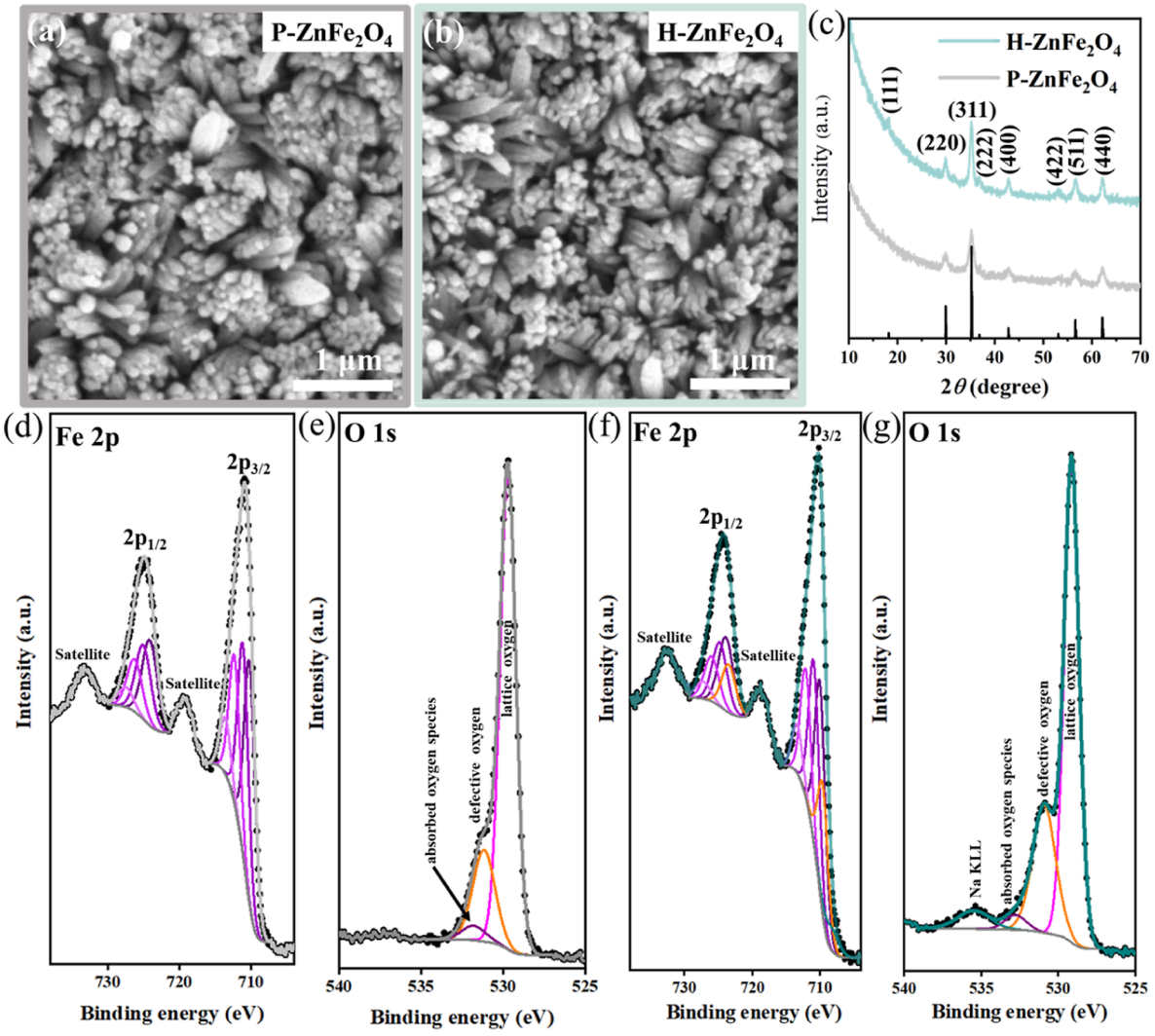

Figure 1. (a,b) Top-view SEM images and (c) XRD patterns of P-$ZnFe_2O_4$ and H-$ZnFe_2O_4$; XP spectra in (d,f) Fe 2p and (e,g) O 1s regions of P-$ZnFe_2O_4$ and H-$ZnFe_2O_4$, respectively. The additional peak observed in (g) located at approximately 535 eV can be ascribed to Na KLL, which is a residue from the washing process used in the synthesis.

the surface of $ZnFe_2O_4$ photoanodes. More importantly, both pristine and hydrogen-treated $ZnFe_2O_4$ exhibit excellent stability in near-neutral (borate buffer electrolyte) and basic electrolyte (KOH) under operando PEC water oxidation conditions. Notably, the dissolution of the hydrogen-reduced $ZnFe_2O_4$ was only found once the applied potential is more cathodic than −0.1 VRHE (vs reversible hydrogen electrode, RHE).

RESULTS AND DISCUSSION

As shown in Figure 1a, pristine nanorod arrays of $ZnFe_2O_4$ (named P-$ZnFe_2O_4$) were successfully synthesized on the fluorine-doped tin oxide (FTO) substrate according to a modified conversion route.[9,21] The obtained pristine sample was later annealed under a pure H_2 atmosphere to introduce oxygen deficiency (named H-$ZnFe_2O_4$). The scanning electron microscope (SEM) micrographs of P-$ZnFe_2O_4$ and H-$ZnFe_2O_4$ (Figure 1a,b) show that hydrogen reduction did not cause any obvious morphological change. Meanwhile, all of the reflections observed in the acquired grazing incidence X-ray diffraction (GIXRD) patterns of the pristine and hydrogen-treated films (Figure 1c) can be assigned to $ZnFe_2O_4$ (JCPDS 22-1012),[13] indicating that hydrogen reduction did not induce notable structural variation to the synthesized $ZnFe_2O_4$ film. Moreover, the optical band gap energies calculated from the Tauc plots (Figure S1) of P-$ZnFe_2O_4$ and H-$ZnFe_2O_4$ show negligible differences, further confirming that H_2 treatment did not cause changes to the bulk absorption properties of $ZnFe_2O_4$.

To gain insight into the effect of H_2 treatment on the surface of $ZnFe_2O_4$, X-ray photoelectron spectroscopy (XPS) analysis was conducted. The ratio of Zn to Fe calculated from the XPS measurement is around 1:2 and 1:3 for P-$ZnFe_2O_4$ and H-$ZnFe_2O_4$ films, respectively, indicating that a leeching of Zn was induced during the hydrogen treatment (Figure S2). For both samples, their spectrum in the Fe 2p region (Figure 1d,f) exhibits two strong and two weak peaks, corresponding to $2p_{3/2}$, $2p_{1/2}$, and their shakeup satellite peaks. It is noteworthy that the components within the $2p_{3/2}$ and $2p_{1/2}$ regions were fitted with a constrained area ratio of 2:1, and a doublet separation of 13.9 eV was found, which is identical to that observed for Fe_3O_4.[28] To further reveal the differences between the two samples, Fe 2p regions were deconvoluted based on the peak shapes developed by Biesinger et al. for

https://doi.org/10.1021/acscatal.4c02186
ACS Catal. 2024, 14, 10789−10795

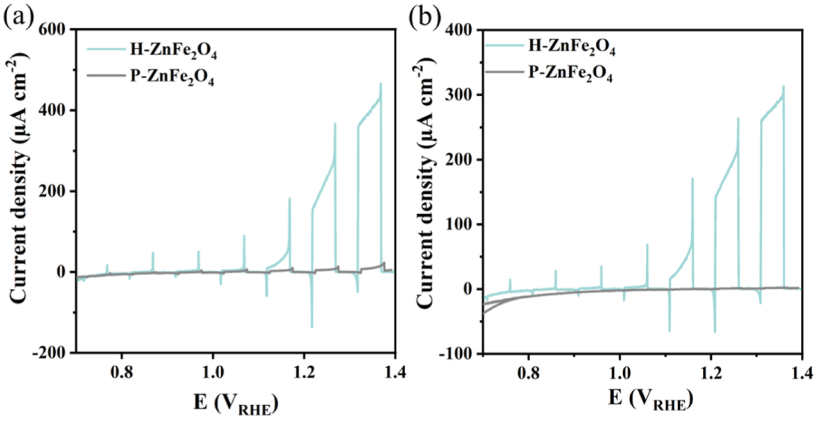

Figure 2. Chopped light voltammetry plots of P-$ZnFe_2O_4$ and H-$ZnFe_2O_4$ without cocatalysts for (a) substrate side illumination and (b) electrolyte side illumination.

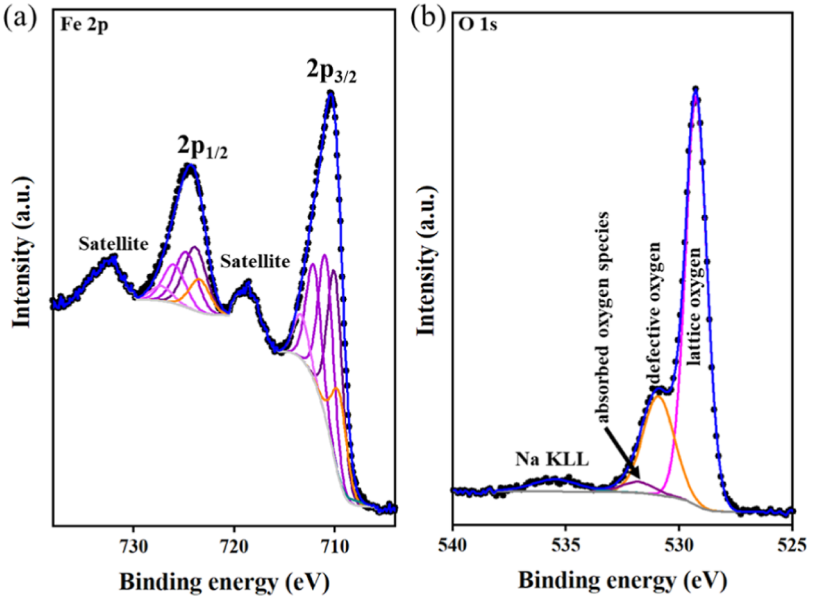

Figure 3. XPS spectra in (a) Fe 2p and (b) the O 1s regions of H-$ZnFe_2O_4$ acquired after the PEC test. The Na KLL is a residue from the washing process used in the synthesis.

$NiFe_2O_4$.[29] Notably, the deconvoluted peaks of P-$ZnFe_2O_4$ fit well to those of $NiFe_2O_4$ except for the first peak located at 710.2 eV, which is 1.2 eV higher than that of $NiFe_2O_4$, but very close to that of the Fe^{3+} species in Fe_3O_4.[28] Regarding the deconvolution of the Fe $2p_{3/2}$ peak of H-$ZnFe_2O_4$, two additional peaks located at 709.6 and 708.4 eV had to be added to obtain a satisfactory peak fit. The one that sits at 709.6 eV is very similar to Fe_2O_3, indicating the existence of an oxidic Fe^{3+} species, which also fits well with the Zn depletion. The other one located at 708.4 eV, which is too small to be discerned, is fitted to the FeO and Fe^{2+} species in $NiFe_2O_4$.[29] Accordingly, we conclude that the H_2 treatment slightly reduces the surficial Fe^{3+}. Moreover, the lattice oxygen (529.7 eV) and defective oxygen (531.2 eV) peaks in the O 1s spectra of P-$ZnFe_2O_4$ are shifted to 529.2 and 530.9 eV after H_2 treatment (Figure 1e,g), indicating a more electron-rich environment of H-$ZnFe_2O_4$, which fits with the additional Fe^{3+} species at lower binding energies compared to P-$ZnFe_2O_4$. The defective/lattice oxygen ratio increases from 0.27 (P-$ZnFe_2O_4$) to 0.41 (H-$ZnFe_2O_4$), demonstrating that the H_2 treatment results in the formation of additional defects.

The PEC performance of P-$ZnFe_2O_4$ and H-$ZnFe_2O_4$ was tested in a 1.0 M NaOH electrolyte to evaluate the effect of H_2 treatment on the catalytic activities of $ZnFe_2O_4$ (Figures 2 and S3). As shown in Figure 2a, owing to its increased donor intensity, the photocurrent of H-$ZnFe_2O_4$ at 1.23 V_{RHE} for substrate side illumination (SSI) is 181 $\mu A/cm^2$, which is much higher than that of P-$ZnFe_2O_4$ (4.72 $\mu A/cm^2$). Meanwhile, the photocurrent density for electrolyte side illumination (ESI) at 1.23 V of H-$ZnFe_2O_4$ is 173 $\mu A/cm^2$ (Figure 2b), only marginally reduced compared to SSI, resulting in an I_{ESI}/I_{SSI} ratio of 0.95, which is significantly higher than that of P-$ZnFe_2O_4$ (0.14). This indicates that H-$ZnFe_2O_4$ has enhanced electrical conductivity.

The Mott−Schottky plots (Figure S4) also indicate that H-$ZnFe_2O_4$ has a higher carrier concentration (lower slope) than P-$ZnFe_2O_4$. However, given the complexity of the nanowires with nonuniform geometry (Figure 1a,b), it is challenging to evaluate the actual surface area of $ZnFe_2O_4$ for proper quantification. Using the geometric surface area of the substrate to normalize, the donor density was evaluated to be on the order of 10^{19} cm^{-3} (P-$ZnFe_2O_4$) to 10^{20} cm^{-3} (H-

https://doi.org/10.1021/acscatal.4c02186
ACS Catal. 2024, 14, 10789−10795

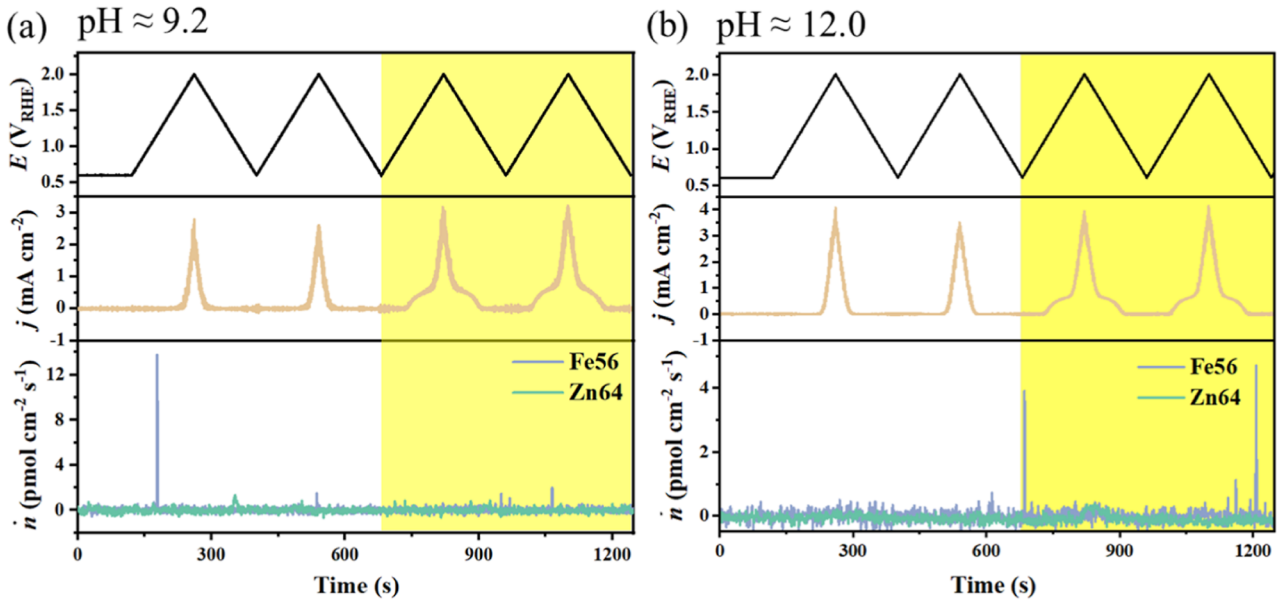

Figure 4. Time profiles of applied potential (E), current density (j), and dissolution rates ($\dot{n}$) of Fe and Zn during the light-off and light-on CV scans of H-$ZnFe_2O_4$ in the (a) borate buffer solution (pH = 9.2) and the (b) KOH solution (pH = 12.0), respectively.

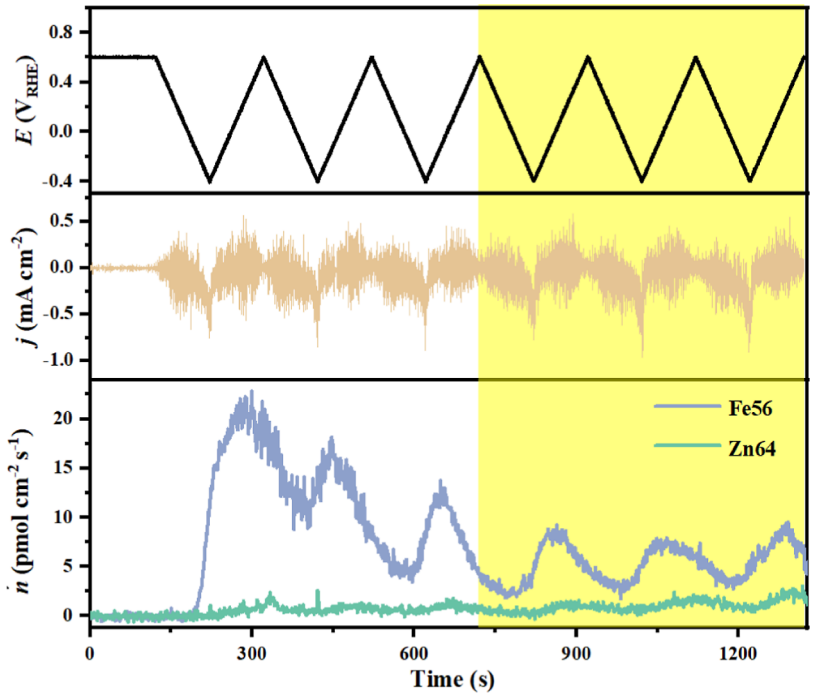

Figure 5. Time profiles of applied potential (E), current density (j), and dissolution rates ($\dot{n}$) of Fe and Zn during the light-off and light-on CV scans of H-$ZnFe_2O_4$ as a cathode in the borate buffer solution.

$ZnFe_2O_4$), which is too high to not consider correction for the capacitance and voltage drop of the Helmholtz layer.[30,31] Refraining from quantitative evaluation, we report only a qualitative comparison between P-$ZnFe_2O_4$ and H-$ZnFe_2O_4$, as the H_2 treatment maintained the morphology of electrodes.

To understand the impact of PEC oxidation on the surface of $ZnFe_2O_4$, XPS analysis (Figures 3 and S5) was conducted on H-$ZnFe_2O_4$ after the PEC tests. As can be seen, the surface of H-$ZnFe_2O_4$ was re-oxidized, which is evident from the decrease in the percentage of peaks in the Fe 2p region. Specifically, the peak at 708.4 eV dropped from 18.3% to 14.8%, and the peak at 709.6 eV decreased from 2.2% to 0.5%. Moreover, the defective/lattice oxygen ratio also decreased from 0.41 to 0.35.

Furthermore, operando iSFC−ICPMS measurements were performed to characterize the stability of $ZnFe_2O_4$ during PEC water oxidation. As shown in Figure 4a, H-$ZnFe_2O_4$ was first put in contact with the borate buffer electrolyte (pH = 9.2) without the application of potential and illumination, and no dissolution was detected, indicating that it is stable in the electrolyte. Then, the potential of H-$ZnFe_2O_4$ was set to 0.6 V_{RHE} for 2 min without detectable dissolution and negligible Faradaic current. Subsequently, the effect of potential and illumination on the H-$ZnFe_2O_4$ was studied (Figures 4a and

https://doi.org/10.1021/acscatal.4c02186
ACS Catal. 2024, 14, 10789−10795

S6) by performing cyclic voltammetry (CV) scans between 0.6 and 2.0 V_{RHE} in the dark and under illumination. An electrocatalytic current of H-$ZnFe_2O_4$ was observed in the dark once the potential was higher than 1.67 V_{RHE}, corresponding to the onset potential of electrocatalytic OER. In contrast, in addition to the electrocatalytic current, a photocurrent was observed while performing the CV scans under illumination with an onset potential of 1.15 V_{RHE}. However, it should be noted that even in the high anodic potential range H-$ZnFe_2O_4$ exhibits good stability without any detectable dissolution under either electrocatalytic or PEC conditions. Furthermore, H-$ZnFe_2O_4$ demonstrated stable PEC activity without any detectable dissolution (Figures 4b and S7) and morphology changes (Figure S8) after testing in the 0.01 M KOH solution (pH = 12.0). Notably, for electrocatalytic OER and PEC in the KOH solution, the onset potential of H-$ZnFe_2O_4$ is 1.63 V_{RHE} and 1.06 V_{RHE}, respectively.

It is noteworthy that under identical testing conditions in both the borate buffer solution and the KOH solution, P-$ZnFe_2O_4$ exhibits similar electrocatalytic OER activity to that of H-$ZnFe_2O_4$ (Figures S9−S11). However, little photocurrent was detected for P-$ZnFe_2O_4$ in the whole scanning potential range. This corresponds well to the lack of PEC activity for P-$ZnFe_2O_4$, especially under ESI (Figure 2b). Notably, a dissolution peak of Zn was observed as the potential was initially set to 0.6 V in the borate buffer solution (Figure S9a). Unlike many spikes, this peak integrates to ∼135 pmol cm^{-2}, corresponding to ∼0.057 nm of $ZnFe_2O_4$. Such an amount of Zn loss, nevertheless, would cause only negligible change to the surface stoichiometry of P-$ZnFe_2O_4$.

To further explore the stability of H-$ZnFe_2O_4$, we extended the CV scan range from 0.6 V_{RHE} to −0.4 V_{RHE} in the borate buffer electrolyte (Figures 5 and S12). The measured current density is low at cathodic potentials, indicating that H-$ZnFe_2O_4$ is almost inert toward hydrogen evolution. Furthermore, as an n-type semiconductor, H-$ZnFe_2O_4$ also does not show a photocurrent at the cathodic potentials. However, in contrast to its good stability as an anode, high dissolution of Zn and Fe was observed when it was used as a cathode. It can be seen that within each cycle, Fe starts to dissolve at around −0.1 V_{RHE} and reaches a maximum at around 0 V_{RHE} in the reverse anodic scan (Figure S12). Meanwhile, the dissolution of Zn starts around −0.4 V_{RHE} when the anodic scan starts and reaches its maximum at around 0.2 V_{RHE} in the reverse anodic scans. Noticeably, in the initial CV cycles, the dissolution rate of Fe is much higher, which corresponds well to an initial Fe-rich surface of H-$ZnFe_2O_4$ (Figure 1). After several CV cycles, the dissolution rate of Zn and Fe becomes more stable, as the surface composition of $ZnFe_2O_4$ evolves closer to the stoichiometric ratio.

The above data indicate that $ZnFe_2O_4$ is stable in basic electrolytes while the applied potential is more anodic than −0.1 V_{RHE} in near-neutral and alkaline electrolytes. However, at more cathodic potentials, the dissolution of Fe and Zn could be observed with onset potentials of −0.1 V_{RHE} and −0.4 V_{RHE}, respectively. This can be understood by comparing the Pourbaix diagrams of Fe and Zn.[32] At acidic pH, Fe and Zn are most stable in the aqueous phase at their divalent states; therefore, $ZnFe_2O_4$ is unstable against dissolution. At neutral and basic pH, Fe and Zn are both stable in solid phases. For Fe, the thermodynamic equilibrium of the redox reaction $Fe_3O_4 \leftrightarrow Fe$ happens at −0.1 V_{RHE}. Note that Fe_3O_4 and $ZnFe_2O_4$ both have the spinel structure, with the latter replacing the Fe^{2+} site with Zn^{2+}. Below −0.1 V_{RHE}, the driving force to reduce surface Fe^{3+} to Fe^0 would change the local coordination environment of Fe, which may lead to subsequent dissolution, as was observed experimentally in this potential range. Similarly, the reduction of Zn^{2+} in the reaction $ZnO \leftrightarrow Zn$ is spontaneous at potentials more cathodic than −0.4 V_{RHE}, which coincides with the range of observed Zn dissolution from $ZnFe_2O_4$. Hence, we have demonstrated that under basic pH conditions, the stability of $ZnFe_2O_4$ follows the same trend as that of the unary Fe−H_2O and Zn−H_2O systems. For compound semiconductors, experimental verification of the aqueous stability is necessary, and we have shown that unary Pourbaix diagrams can serve well for initial estimation.

CONCLUSIONS

In summary, to analyze the activity and stability of H-$ZnFe_2O_4$ and P-$ZnFe_2O_4$ photoanodes under alkaline PEC conditions, an iSFC−ICPMS setup was applied to monitor their dynamic dissolution rates while measuring the catalytic performance. While H-$ZnFe_2O_4$ is more active than P-$ZnFe_2O_4$, neither Zn nor Fe was detected in the basic electrolyte under PEC OER conditions for both of them. This confirms that hydrogen treatment can enhance the activity of $ZnFe_2O_4$ without compromising stability under alkaline PEC OER conditions. Meanwhile, it was found that by biasing H-$ZnFe_2O_4$ to cathodic potentials, Fe and Zn dissolution can be triggered at potentials more cathodic than −0.1 V_{RHE} and −0.4 V_{RHE}, respectively. We hence conclude that at basic pH, H-$ZnFe_2O_4$ is stable in PEC operations at potentials more anodic than −0.1 V_{RHE}.

MATERIALS AND METHODS

Materials. Iron(III) chloride hexahydrate ($FeCl_3$·6 H_2O), sodium nitrate ($NaNO_3$), zinc nitrate hexahydrate ($Zn(NO_3)_2$ 6 H_2O), and potassium hydroxide were purchased from Sigma-Aldrich, Grüssing, and Carl Roth, respectively. All the chemicals were used as received without any further purification. FTO substrates (Pilkington TEC 8 glass with a sheet resistance of 8 Ω) were purchased from XOP-Glass. Before usage, they were sequentially ultrasonicated in ethanol, acetone, isopropyl alcohol, and ultrapure water for 20 min.

Preparation of P-$ZnFe_2O_4$ and H-$ZnFe_2O_4$. The P-$ZnFe_2O_4$ thin film was prepared according to the previously reported methods.[8,9] First, a precursor solution of 0.15 M $FeCl_3$·6 H_2O and 1 M $NaNO_3$ in ultrapure water was prepared in a glass bottle. Second, the cleansed FTO substrate was placed in the bottle and kept in a preheated oven for 3 h at 100 °C. Afterward, the FTO substrate was taken out, thoroughly rinsed with ultrapure water, and dried under a nitrogen stream. The dried substrate was then placed on a 100 °C heating plate and coated drop-by-drop with an aqueous 0.1 M $Zn(NO_3)_2$ solution. Subsequently, the wetted substrate was transferred to a preheated muffle furnace for 20 min at 600 °C. Then, to remove the formed ZnO skin, the coated dry substrate was kept soaking in a 5 M NaOH solution for 4 h. Finally, the substrate was rinsed with ultrapure water and dried under a nitrogen stream. For H-$ZnFe_2O_4$, the P-$ZnFe_2O_4$ thin film was placed in a tubular oven under pure hydrogen flow for 1 h. The temperature of 200 °C and the hydrogen flow rate of 160 mL/min were set according to the publication of Kim et al.[15]

https://doi.org/10.1021/acscatal.4c02186
ACS Catal. 2024, 14, 10789−10795

Characterization. SEM micrographs were taken at 5 kV on a Scios 2 microscope by using the secondary electron detector. X-ray diffraction (XRD) of the thin films was performed on a Rigaku SmartLab diffractometer equipped with a rotating copper anode at 200 mA and 45 kV. For the detection, a HyPix-3000 2D detector was used. The data was recorded in the range of 10 to 70° 2θ with a scan rate of 3° min^{-1} and a step size of 0.016°, while the incidence angle ω was fixed at 0°. XPS was performed with a VersaProbe III Scanning XPS Microprobe (Physical Electronics PHI) using monochromatic Al Kα radiation with a beam diameter of 200 μm. A step size of 0.4 eV and a pass energy of 224 eV were used for acquiring the survey spectra. Regarding the high-resolution spectra, the step size and pass energy were 0.1 and 26 eV, respectively. In both cases, the step time was 50 ms. Sample charging was prevented by using slow-moving Ar ions and an electron flood gun. Sputter cleaning was not performed on the samples before measurements to prevent sample reduction due to preferential sputtering. The obtained XPS data were analyzed with CasaXPS using Gaussian−Lorentzian (GL30) line shapes and Shirley backgrounds. Moreover, for charge correction, the CC/CH peaks of the C 1s spectra were set to 284.8 eV. The ultraviolet−visible spectroscopy (UV−vis) tests were performed on a PerkinElmer Lambda 750 spectrometer with a 100 mm integrating sphere equipped with an InGaAs detector. The pseudoabsorption spectra were plotted after the Kubelka−Munk theory. As a reference for high reflection, a $BaSO_4$ white standard was used. An uncoated FTO substrate was used as a reference for the measurements in transmission mode.

PEC Measurement. As shown in Figure S13, all PEC measurements were conducted in a PEC cell consisting of an Ag/AgCl (3 M NaCl), a platinum wire, and the studied film as the reference, counter, and working electrodes, respectively. For the preparation of the working electrode, copper wire was stuck onto an uncoated part of the substrate with adhesive and conductive copper tape. The illuminated area of the working electrode is 10 mm^2. The applied potentials against the Ag/AgCl reference electrode were converted to the RHE scale via the Nernst equation. The electrolyte used is 1 M NaOH (measured pH = 13.256). The current densities were calculated with regard to the geometric surface area of the working electrodes, which is 10 mm^2 in PEC measurements and 1 mm^2 in operando iSFC−ICPMS measurements. The potentiostat used here is a Zahner Zennium CIMPS-PCS system. The current densities were assessed based on the light source is a Quantum Design LOT sun simulator with an AM 1.5 G filter and a 300 W Xe lamp of an intensity of 100 mW/cm^2. The illuminated area of the photoanode was 10 mm^2. Electrochemical impedance measurements were conducted without illumination for a range of applied potentials with an amplitude of 20 mV. The geometric area of the substrate was 1 cm^2. The frequency was varied from 1 Hz to 100 kHz with ten measuring points per decade, and the plotted data were taken from 1 kHz values.

iSFC−ICPMS Measurement. PEC tests were performed on a Reference600 potentiostat (Gamry) with a scanning flow cell. P-$ZnFe_2O_4$ and H-$ZnFe_2O_4$ were used as the working electrodes and the working area was confined to 1 mm^2 by the iSFC. A Pt wire (0.5 mm) and an Ag/AgCl electrode in 3.0 M KCl were used as the counter electrode and reference electrode, respectively. A borate buffer prepared from $Na_2B_4O_7$ (15 mM, Merck) with a pH value around 9.2 and a KOH solution (prepared from KOH Suprapur, Merck) with a pH value around 12 was used as the electrolyte, respectively. A daily measurement of the electrolyte was performed on a MultiLab540 pH meter to guarantee the accuracy of the potential value on the RHE scale. ESI of the working electrode was achieved using a Superlite S04 light (Lumatec), which was filtered to 400−700 nm and calibrated to a power intensity of 100 mW/cm^2. The dynamic time-resolved electrolyte analysis was done on a NexION300X ICPMS (PerkinElmer) by pumping the electrolyte through the iSFC with a flow rate of 3.4 μL/s. For quantitative analysis, the detected intensities were analyzed with respect to an internal standard of ^{74}Ge for compensation of the physical interferences.

■ ASSOCIATED CONTENT

Supporting Information

The Supporting Information is available free of charge at https://pubs.acs.org/doi/10.1021/acscatal.4c02186.

UV−vis transmission spectra, Tauc plots, XPS survey spectra, chopped light voltammetry plots, Mott−Schottky plots, iSFC-ICPMS results, SEM images, and optical photo of the PEC cell (PDF)

■ AUTHOR INFORMATION

Corresponding Authors

Ningyan Cheng − *Max-Planck-Institut für Eisenforschung, Düsseldorf 40237, Germany*; orcid.org/0009-0009-7844-3120; Email: n.cheng@mpie.de

Roland Marschall − *Chair of Physical Chemistry III, University of Bayreuth, Bayreuth 95447, Germany*; Email: roland.marschall@uni-bayreuth.de

Siyuan Zhang − *Max-Planck-Institut für Eisenforschung, Düsseldorf 40237, Germany*; orcid.org/0000-0001-7045-0865; Email: siyuan.zhang@mpie.de

Authors

Leonie Kanzler − *Chair of Physical Chemistry III, University of Bayreuth, Bayreuth 95447, Germany*

Yiqun Jiang − *Max-Planck-Institut für Eisenforschung, Düsseldorf 40237, Germany*

Andrea M. Mingers − *Max-Planck-Institut für Eisenforschung, Düsseldorf 40237, Germany*

Morten Weiss − *Chair of Physical Chemistry III, University of Bayreuth, Bayreuth 95447, Germany*

Christina Scheu − *Max-Planck-Institut für Eisenforschung, Düsseldorf 40237, Germany*

Complete contact information is available at: https://pubs.acs.org/10.1021/acscatal.4c02186

Author Contributions

The manuscript was written through the contributions of all authors. All authors have approved the final version of the manuscript.

Funding

Open access funded by Max Planck Society.

Notes

The authors declare no competing financial interest.

■ ACKNOWLEDGMENTS

The authors thank the Key Lab "Device Engineering" of the Bavarian Polymer Institute BPI for the XPS measurement and Dr. Jana Timm for her support on GIXRD. N.C. is grateful for financial support from the Alexander von Humboldt

Foundation. R.M. and S.Z. acknowledge funding from the German Research Foundation (DFG) under the framework of the priority program 2370 (project numbers: 501901537, 502202153). R.M. acknowledges funding by the DFG in the Major Research Instrumentation funding program, project INST 91/459-1 (project no. 468685973).

REFERENCES

(1) Yang, W.; Prabhakar, R. R.; Tan, J.; Tilley, S. D.; Moon, J. Strategies for enhancing the photocurrent, photovoltage, and stability of photoelectrodes for photoelectrochemical water splitting. *Chem. Soc. Rev.* **2019**, *48*, 4979−5015.

(2) Walter, M. G.; Warren, E. L.; McKone, J. R.; Boettcher, S. W.; Mi, Q.; Santori, E. A.; Lewis, N. S. Solar water splitting Cells. *Chem. Rev.* **2010**, *110*, 6446−6473.

(3) Sivula, K.; van de Krol, R. Semiconducting materials for photoelectrochemical energy conversion. *Nat. Rev. Mater.* **2016**, *1*, 15010.

(4) Lee, D. K.; Lee, D.; Lumley, M. A.; Choi, K.-S. Progress on ternary oxide-based photoanodes for use in photoelectrochemical cells for solar water splitting. *Chem. Soc. Rev.* **2019**, *48*, 2126−2157.

(5) Balu, S.; Chen, Y.; Chen, S.-W.; Yang, T. C.-K. Rational synthesis of $Bi_xFe_{1-x}VO_4$ heterostructures impregnated sulfur-doped g-C_3N_4: A visible-light-driven type-II heterojunction photo(electro)catalyst for efficient photodegradation of roxarsone and photoelectrochemical OER reactions. *Appl. Catal., B* **2022**, *304*, 120852.

(6) Cui, J.; Daboczi, M.; Regue, M.; Chin, Y.; Pagano, K.; Zhang, J.; Isaacs, M. A.; Kerherve, G.; Mornto, A.; West, J.; Gimenez, S.; Kim, J.-S.; Eslava, S. 2D bismuthene as a functional interlayer between $BiVO_4$ and NiFeOOH for enhanced oxygen-evolution photoanodes. *Adv. Funct. Mater.* **2022**, *32*, 2207136.

(7) Pastor, E.; Sachs, M.; Selim, S.; Durrant, J. R.; Bakulin, A. A.; Walsh, A. Electronic defects in metal oxide photocatalysts. *Nat. Rev. Mater.* **2022**, *7*, 503−521.

(8) Liu, Y.; Xia, M.; Yao, L.; Mensi, M.; Ren, D.; Grätzel, M.; Sivula, K.; Guijarro, N. Spectroelectrochemical and chemical evidence of surface passivation at zinc ferrite ($ZnFe_2O_4$) photoanodes for solar water oxidation. *Adv. Funct. Mater.* **2021**, *31*, 2010081.

(9) Zhu, X.; Guijarro, N.; Liu, Y.; Schouwink, P.; Wells, R. A.; le Formal, F.; Sun, S.; Gao, C.; Sivula, K. Spinel structural disorder influences solar-water-splitting performance of $ZnFe_2O_4$ nanorod photoanodes. *Adv. Mater.* **2018**, *30*, 1801612.

(10) Skliri, E.; Miao, J.; Xie, J.; Liu, G.; Salim, T.; Liu, B.; Zhang, Q.; Armatas, G. S. Assembly and photochemical properties of mesoporous networks of spinel ferrite nanoparticles for environmental photocatalytic remediation. *Appl. Catal., B* **2018**, *227*, 330−339.

(11) She, X.; Zhang, Z.; Baek, M.; Yong, K. Photoelectrochemical enhancement of $ZnO/BiVO_4/ZnFe_2O_4$/rare earth oxide hetero-nanostructures. *Appl. Surf. Sci.* **2018**, *429*, 29−36.

(12) Xiong, K.; Wang, K.; Chen, L.; Wang, X.; Fan, Q.; Courtois, J.; Liu, Y.; Tuo, X.; Yan, M. Heterostructured $ZnFe_2O_4/Fe_2TiO_5/TiO_2$ composite nanotube arrays with an improved photocatalysis degradation efficiency under simulated sunlight irradiation. *Nano-Micro Lett.* **2018**, *10*, 17.

(13) Kirchberg, K.; Wang, S.; Wang, L.; Marschall, R. Mesoporous $ZnFe_2O_4$ photoanodes with template-tailored mesopores and temperature-dependent photocurrents. *ChemPhysChem* **2018**, *19*, 2313−2320.

(14) Hufnagel, A. G.; Peters, K.; Müller, A.; Scheu, C.; Fattakhova-Rohlfing, D.; Bein, T. Zinc ferrite photoanode nanomorphologies with favorable kinetics for water-splitting. *Adv. Funct. Mater.* **2016**, *26*, 4435−4443.

(15) Kim, J. H.; Jang, Y. J.; Kim, J. H.; Jang, J. W.; Choi, S. H.; Lee, J. S. Defective $ZnFe_2O_4$ nanorods with oxygen vacancy for photoelectrochemical water splitting. *Nanoscale* **2015**, *7*, 19144−19151.

(16) Simon, C.; Zakaria, M. B.; Kurz, H.; Tetzlaff, D.; Blösser, A.; Weiss, M.; Timm, J.; Weber, B.; Apfel, U.-P.; Marschall, R. Magnetic $NiFe_2O_4$ nanoparticles prepared via non-aqueous microwave-assisted synthesis for application in electrocatalytic water oxidation. *Chem.—Eur. J.* **2021**, *27*, 16990−17001.

(17) Zander, J.; Weiss, M.; Marschall, R. Fast and facile microwave synthesis of cubic $CuFe_2O_4$ nanoparticles for electrochemical CO_2 reduction. *Adv. Energy Sustainability Res.* **2023**, *4*, 2200184.

(18) Granone, L. I.; Ulpe, A. C.; Robben, L.; Klimke, S.; Jahns, M.; Renz, F.; Gesing, T. M.; Bredow, T.; Dillert, R.; Bahnemann, D. W. Effect of the degree of inversion on optical properties of spinel $ZnFe_2O_4$. *Phys. Chem. Chem. Phys.* **2018**, *20*, 28267−28278.

(19) Dolcet, P.; Kirchberg, K.; Antonello, A.; Suchomski, C.; Marschall, R.; Diodati, S.; Muñoz-Espí, R.; Landfester, K.; Gross, S. Exploring wet chemistry approaches to $ZnFe_2O_4$ spinel ferrite nanoparticles with different inversion degrees: a comparative study. *Inorg. Chem. Front.* **2019**, *6*, 1527−1534.

(20) Cai, L.; Guo, J.; Liu, T.; Tian, J.; Wang, Z.; Liu, Y.; Hamdy, M. S.; Sun, X. Selective photo-reduction of nitrate to nitrogen with a two-step process by a KBH_4/Cu(II) modified $CuFe_2O_4$ photocatalyst. *Nano Res.* **2023**, *16*, 10462−10475.

(21) Guijarro, N.; Bornoz, P.; Prévot, M.; Yu, X.; Zhu, X.; Johnson, M.; Jeanbourquin, X.; le Formal, F.; Sivula, K. Evaluating spinel ferrites MFe_2O_4 (M = Cu, Mg, Zn) as photoanodes for solar water oxidation: prospects and limitations. *Sustainable Energy Fuels* **2018**, *2*, 103−117.

(22) Zhang, S.; Ahmet, I.; Kim, S.; Kasian, O.; Mingers, A. M.; Schnell, P.; Kölbach, M.; Lim, J.; Fischer, A.; Mayrhofer, K. J. J.; Cherevko, S.; Gault, B.; van de Krol, R.; Scheu, C. Different photostability of $BiVO_4$ in near-pH-neutral electrolytes. *ACS Appl. Energy Mater.* **2020**, *3*, 9523−9527.

(23) Aymerich-Armengol, R.; Vega-Paredes, M.; Wang, Z.; Mingers, A. M.; Camuti, L.; Kim, J.; Bae, J.; Efthimiopoulos, I.; Sahu, R.; Podjaski, F.; Rabe, M.; Scheu, C.; Lim, J.; Zhang, S., Operando Insights on the Degradation Mechanisms of Rhenium doped Molybdenum Disulfide Nanocatalysts for Electrolyzer Applications. *Appl. Phys.* **2023**, arXiv:2309.08977.

(24) Myers, D. J.; Wang, X.; Smith, M. C.; More, K. L. Potentiostatic and potential cycling dissolution of polycrystalline platinum and platinum nano-particle fuel cell catalysts. *J. Electrochem. Soc.* **2018**, *165*, F3178−F3190.

(25) Knöppel, J.; Zhang, S.; Speck, F. D.; Mayrhofer, K. J. J.; Scheu, C.; Cherevko, S. Time-resolved analysis of dissolution phenomena in photoelectrochemistry - a case study of WO_3 photocorrosion. *Electrochem. Commun.* **2018**, *96*, 53−56.

(26) Zhang, S.; Rohloff, M.; Kasian, O.; Mingers, A. M.; Mayrhofer, K. J. J.; Fischer, A.; Scheu, C.; Cherevko, S. Dissolution of $BiVO_4$ photoanodes revealed by time-resolved measurements under photo-electrochemical conditions. *J. Phys. Chem. C* **2019**, *123*, 23410−23418.

(27) Benavente Llorente, V.; Jenewein, K. J.; Bierling, M.; Körner, A.; Hutzler, A.; Kormányos, A.; Cherevko, S. Photocorrosion of hematite photoanodes in neutral and alkaline electrolytes. *J. Phys. Chem. C* **2023**, *127*, 19687−19697.

(28) Mills, P.; Sullivan, J. L. A Study of the core level electrons in iron and its three oxides by means of X-ray photoelectron spectroscopy. *J. Phys. D: Appl. Phys.* **1983**, *16*, 723−732.

(29) Biesinger, M. C.; Payne, B. P.; Grosvenor, A. P.; Lau, L. W. M.; Gerson, A. R.; Smart, R. S. C. Resolving surface chemical states in XPS analysis of first row transition metals, oxides and hydroxides: Cr, Mn, Fe, Co and Ni. *Appl. Surf. Sci.* **2011**, *257*, 2717−2730.

(30) Sivula, K. Mott-Schottky analysis of photoelectrodes: sanity checks are needed. *ACS Energy Lett.* **2021**, *6*, 2549−2551.

(31) Hankin, A.; Bedoya-Lora, F. E.; Alexander, J. C.; Regoutz, A.; Kelsall, G. H. Flat band potential determination: avoiding the pitfalls. *J. Mater. Chem. A* **2019**, *7*, 26162−26176.

(32) Pourbaix, M. *Atlas of Electrochemical Equilibria*; National Association of Corrosion Engineers: Houston, Texas, 1974.

https://doi.org/10.1021/acscatal.4c02186
ACS Catal. 2024, 14, 10789−10795